J Mater Sci (2015) 50:4083–4094
DOI 10.1007/s10853-015-8964-6

Template-assisted synthesis of core–shell α-Fe_2O_3@TiO_2 nanorods and their photocatalytic property

Ming Chen[1] · Xiao Shen[1] · Qianhui Wu[1] · Wei Li[1] · Guowang Diao[1]

Received: 12 December 2014 / Accepted: 10 March 2015 / Published online: 24 March 2015

Abstract Novel core–shell α-Fe_2O_3@TiO_2 composites were synthesized using α-FeOOH nanorods as hard template via a facile hydrothermal process. The as-prepared α-Fe_2O_3@TiO_2 composites were characterized by transmission electron microscopy, scanning electron microscopy, and X-ray powder diffraction. The effects of various experimental parameters, including thickness of TiO_2 coating and calcination temperature on the morphologies of the resulted products, were systematically investigated. Then, the photocatalytic degradation Rhodamine B (RhB) is chosen as a model reaction to evaluate the catalytic performance of the as-prepared α-Fe_2O_3@TiO_2 composites. The results confirmed that the present core–shell α-Fe_2O_3@TiO_2 composite nanorods exhibit the efficient optical response and the photocatalytic activity from the ultraviolet to the visible region. The thickness and crystal structure of TiO_2 affect the photocatalytic activity. The proposed synthesis strategy might provide a facile and effective method for developing noble semiconductors core–shell architecture nanocomposites.

Introduction

Titanium dioxide (TiO_2), as one of the most important transition-metal oxides, has attracted extensive attention for its superior physical and chemical properties and exhibits wide potential applications in various fields such as solar energy conversion [1, 2], water purification and treatment [3–5]. TiO_2 is a common choice for photocatalyst candidates owing to its high photocatalytic activity, excellent chemical stability, low cost, and nontoxicity. However, due to its wide band gap energy of 3.0–3.2 eV, TiO_2 is active only under near-ultraviolet irradiation [6–8]. From the viewpoint of utilizing solar light, visible light responsive TiO_2-based photocatalysts are highly desired [9–12]. Moreover, TiO_2 has a relatively high electron–hole recombination rate, which will decrease its photoactivity [13–15].

To solve these issues and further improve the photocatalytic performance of TiO_2 catalysts in the visible region, the optical absorption of TiO_2 catalysts must be adjusted to shift from the UV region to the visible-light region, enabling more photons to be absorbed and utilized in decomposing the pollutants, and the photogenerated electrons and holes must be separated into different positions on the catalysts. The advancement of the visible light response of TiO_2 and decrease of the recombination rate of the photogenerated electrons and holes can be achieved by doping transition metal [16–18], inorganic dye-sensitizing [19, 20], valuable metal deposition [21–25], and coupling titania with other semiconductors [26–31].

Recently, core–shell nanocomposites have received significant attention owing to their importance in diverse fields of dye-sensitized solar cells [32], composite catalysts [33], energy storage and conversion [34, 35], and gas sensors [36]. The synthesis methods of core–shell nanocomposites include simultaneous fabrication [37, 38], sequential fabrication [39, 40], and displacement reaction fabrication [41, 42]. Inspiringly, coupling titania with other semiconductors core–shell architecture nanocomposites afford a possible solution as a result of the synergy to

✉ Ming Chen
chenming@yzu.edu.cn

✉ Guowang Diao
gwdiao@yzu.edu.cn

[1] College of Chemistry and Chemical Engineering, Yangzhou University, Yangzhou 225002, People's Republic of China

improve the photocatalytic performance of TiO_2 catalysts. TiO_2-based photocatalytic heterostructures or nanocomposites such as noble metal/TiO_2 [21–25, 32], carbon/TiO_2 [43, 44], metal oxide/TiO_2 [45–47], and metal chalcogenide/TiO_2 [48] have been proposed and studied. The previously reported TiO_2-based nanocomposites display a greatly enhanced photocatalytic performance in organic pollutant degradation in the visible light region. Among these semiconductor nanomaterials, hematite (α-Fe_2O_3), an *n*-type semiconductor ($E_g = 2.1$ eV), is the most thermodynamic stable species of iron oxides. Hematite has been intensively researched in Li-ion batteries [35], water splitting [49], environmental treatment [50, 51], and optical devices because of its favorable band gap, abundance, stability, biodegradability, low cost, and nontoxicity. α-Fe_2O_3/metal oxide heterostructures, such as α-Fe_2O_3/Ag/SnO_2 [52], α-Fe_2O_3/ZnO [53], α-Fe_2O_3/CdS [54], and α-Fe_2O_3/TiO_2 [55–58] can decrease the recombination rate of photogenerated electrons and holes [52–54]. Furthermore, the α-Fe_2O_3/metal oxide heterostructures can be used to improve the visible light response of nanocomposites [52–58].

Herein, we reported a new method to synthesize α-Fe_2O_3@TiO_2 composites based on hard template-assisted method. In this paper, α-FeOOH nanorods act as hard templates to fabricate core–shell α-Fe_2O_3@TiO_2 composite nanorods with different shell thicknesses. Then, the photocatalytic degradation Rhodamine B (RhB) is chosen as a model reaction to evaluate the catalytic performance of the as-prepared α-Fe_2O_3@TiO_2 composites under the irradiation of UV and visible light. The present core–shell α-Fe_2O_3@TiO_2 composite nanorods exhibit good photocatalytic activity.

Experimental section

Materials

$FeCl_3 \cdot 6H_2O$, tetrabutyl titanate (TBOT), RhB, NaOH, and concentrated ammonia solution (28 wt%) were of analytical grade and purchased from Sinopharm Co. Other chemicals and solvents are reagent grade and commercially available. Deionized water was used for all experiments.

Characterization

Transmission electron microscopy (TEM) observation was conducted on a Philips TECNAI-12 instrument. Scanning electron microscopy (SEM) was applied to investigate the morphologies of samples, which were carried out with Hitachi S-4800 (Japan). X-ray diffraction (XRD) data were obtained with a graphite monochromator and Cu Kα radiation ($\lambda = 0.1541$ nm) on a D8 advance superspeed powder diffractometer (Bruker). The energy-dispersive X-ray (EDX) analysis was performed on a KEVEX X-ray energy detector. Fourier transform infrared (FTIR) spectra for the various samples were recorded on a Bruker Tensor 27 spectrometer operated at a resolution of 4 cm^{-1}. Carefully weighed quantities of the different samples were subjected to thermogravimetric analysis (TGA) on a STA409PC (NETZSCH) TGA instrument at a heating rate of 10 °C min^{-1} under vacuum from 30 to 600 °C. Ultraviolet–Visible (UV–Vis) diffuse reflectance spectra (DRS) were recorded with an UV–Vis spectrophotometer using $BaSO_4$ as the reference (Shimadzu, UV-3600). UV–Vis absorption spectra were taken by a Shimazu UV-2501 double-beam spectra photometer.

Preparation of core–shell α-Fe_2O_3@TiO_2 composites

Synthesis of α-FeOOH nanorods

In a typical process, $FeCl_3 \cdot 6H_2O$ (0.675 g) and NaOH (0.5 g) were dissolved in 50 mL H_2O under mechanical stirring. Then the mixture was loaded into a Teflon-lined stainless steel autoclave of 50 mL capacity. The autoclave was sealed and maintained at 180 °C for 24 h and then cooled to room temperature naturally. Then, the yellow precipitates were separated and collected by centrifugation, followed by washing with deionized water and ethanol for 3 times, respectively.

Synthesis of α-Fe_2O_3@TiO_2 core–shell composite nanorods

The uniform TiO_2 shell core–shell structures were prepared via the versatile kinetics-controlled coating method [59]. The α-FeOOH nanorods (0.075 g) were dispersed in absolute ethanol (100 mL), and mixed with concentrated ammonia solution (0.30 mL, 28 wt%) under ultrasound for 15 min. Then 1.0 mL of TBOT was added dropwise in 5 min, and the reaction was allowed to proceed for 24 h at 45 °C under continuous mechanical stirring. The resultant products were separated and collected, followed by washing with deionized water and ethanol for 3 times, respectively. Then, the obtained powders were dried at 65 °C for 24 h. The final product was obtained after calcination at 500 °C for 3 h.

Photocatalytic activity test

The photocatalytic activities of the samples were evaluated by the degradation of RhB in an aqueous solution under the irradiation of ultraviolet (UV) light and visible light. The reactions were conducted at ambient temperature and

pressure. A 300 W Hg lamp (wavelength <400 nm) was employed as UV light source to trigger the photocatalytic reactions. A 250 W Xe lamp (wavelength >420 nm) was employed as simulated sunlight source. Typically, the Hg lamp was positioned 10 cm away from the reactor. The prepared α-Fe_2O_3@TiO_2 composites (0.05 g) were dispersed in a 100 mL of RhB aqueous solution ($c_0 = 1.5 \times 10^{-5}$ mol L^{-1}) in a reaction cell. Before irradiation, the suspensions were magnetically stirred in the dark for 40 min to achieve an adsorption–desorption equilibrium between the dye molecules and catalysts. The suspension was magnetically stirred before and during the illumination. At given time intervals, 3 mL solution was drawn from the reaction system. After centrifugation, the residual concentration of RhB was detected at the maximum absorption wavelength (553 nm) of RhB in the UV–Vis spectrum based on Lambert–Beer's law.

Results and discussion

Characterization of core–shell α-Fe_2O_3@TiO_2 composite nanorods

The morphologies of α-FeOOH nanorods, core–shell α-FeOOH@TiO_2 nanorods, and core–shell α-Fe_2O_3@TiO_2 nanorods were characterized using TEM. α-FeOOH nanorods were first synthesized with a diameter of ~75 nm and length of' ~1 μm as the hard templates (Fig. 1a). Then, via a sol–gel reaction of TBOT (added 0.75 mL) in ethanol/ammonia mixtures, core–shell α-FeOOH@TiO_2 nanorods (labeled as α-FeOOH@TiO_2-0.75) were obtained with a diameter of ~140 nm (Fig. 1b). The thickness of amorphous TiO_2 shell is ~30 nm (inset of Fig. 1b). Last, after calcination of α-FeOOH@TiO_2-0.75 at 500 °C, a new style core–shell structure of the α-Fe_2O_3@TiO_2 composite (labeled as α-Fe_2O_3@TiO_2-0.75) is shown in Fig. 1c. After calcination, the dehydration of α-FeOOH nanorods led to some hollows on the surface of nanorods. On the other hand, hydrous titanium oxide loses H_2O molecules and forms TiO_2 nanoparticles (average diameter is about 20 nm), which are coated on the surface of α-Fe_2O_3 nanorods.

The morphologies of α-FeOOH nanorods, core–shell α-FeOOH@TiO_2 nanorods, and core–shell α-Fe_2O_3@TiO_2 nanorods are also confirmed by SEM. In Fig. 1d, α-FeOOH shows rod-shape structure with the smooth surface. The core–shell α-FeOOH@TiO_2 displays some degree of adhesion among these nanorods (Fig. 1e). Compared with α-FeOOH@TiO_2, TiO_2 nanoparticles are coated on the surface of α-Fe_2O_3 nanorods and the surface roughness increases (Fig. 1f).

The chemical composition of these samples was analyzed by XRD. In Fig. 2a, all the identified diffraction peaks are assigned to the phase pure α-FeOOH (JCPDS Card No. 29-0713). When the amorphous TiO_2 is coated on α-FeOOH (Fig. 2b), XRD pattern still shows the diffraction peaks of α-FeOOH, indicating the thin layer of TiO_2

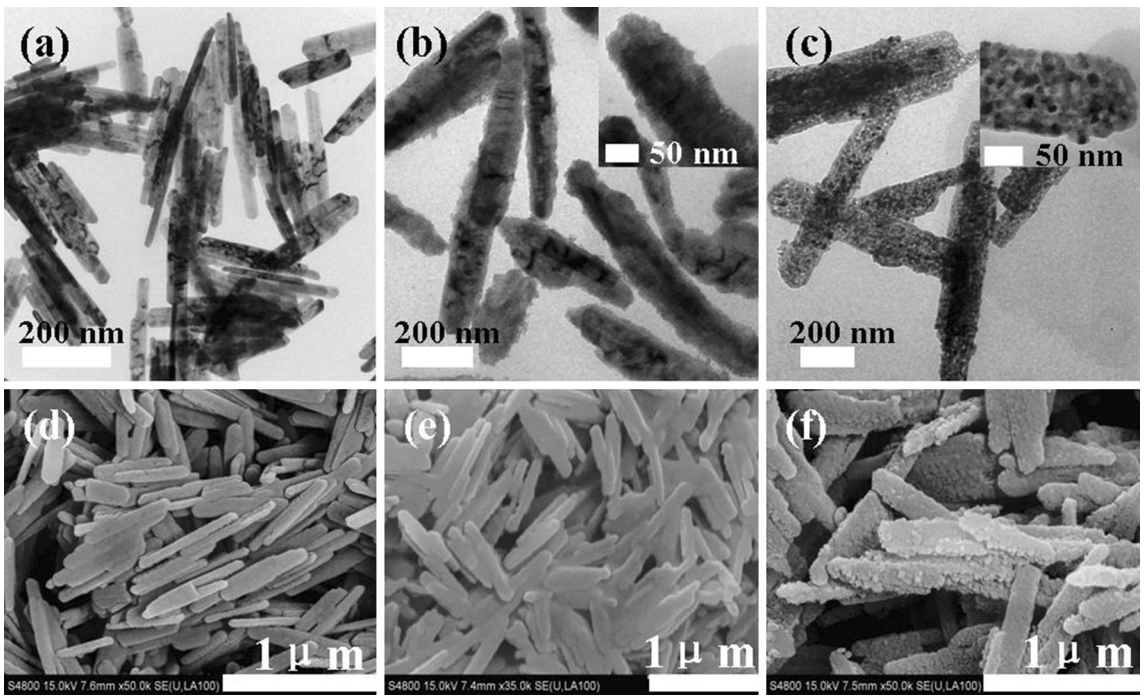

Fig. 1 TEM and SEM images of **a**, **d** α-FeOOH, **b**, **e** α-FeOOH@TiO_2-0.75, **c**, **f** α-Fe_2O_3@TiO_2-0.75

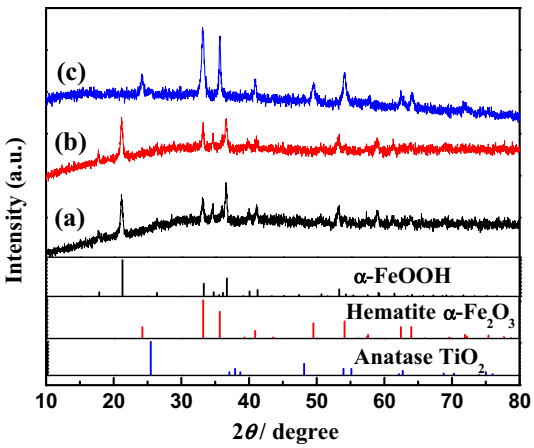

Fig. 2 XRD patterns of *a* α-FeOOH, *b* α-FeOOH@TiO_2-0.75, *c* α-Fe_2O_3@TiO_2-0.75. The *vertical lines* are the standard XRD patterns of α-FeOOH (JCPDS Card No. 29-0713) (*black line*), hematite α-Fe_2O_3 (JCPDS Card No. 33-0664) (*red line*), and anatase TiO_2 (JCPDS Card No. 21-1272) (Color figure online)

coating. After calcinations (Fig. 2c), except 25.2° diffraction peak, the identified diffraction peaks are attributed to the phase pure rhombohedral Fe_2O_3 (JCPDS Card No. 33-0664). The peak at 25.2° corresponds well with the (101) diffraction of anatase TiO_2 (JCPDS Card No. 21-1272).

Figure 3 shows the FTIR spectra of (a) α-FeOOH, (b) α-FeOOH@TiO_2-0.75, (c) α-Fe_2O_3@TiO_2-0.75 composites. For α-FeOOH nanorods (Fig. 3a), the broad peak at 3125 cm^{-1} is attributable to the stretching mode of the bulk hydroxyl groups in the goethite structure (ν_{OH}). The two peaks at 896 and 795 cm^{-1} are assigned to the bending modes of the bulk hydroxyl groups in (δ_{OH}) and out (γ_{OH}) of the (001) plane. In curve b, the typical FTIR spectrum of α-FeOOH@TiO_2-0.75 is similar to the spectrum of α-FeOOH nanorods. However, after calcinations of α-FeOOH@TiO_2-0.75, the strong absorption peak at 529 cm^{-1} corresponds to the Fe–O vibrations, confirming the forming of hematite α-Fe_2O_3.

TGA was used to determine the dehydration process of (a) α-FeOOH and (b) α-FeOOH@TiO_2-0.75. In Fig. 3b, curve a displays the weight loss of α-FeOOH. Only one weight loss step ranging from 200 to 315 °C is due to the intramolecular dehydration. However, for α-FeOOH @TiO_2-0.75 (curve b), two main steps of weight loss shown in curve b are observed. The first step ranging from 25 to 305.9 °C corresponds to the loss of adsorption moisture and intramolecular dehydration of α-FeOOH, and the condensation of residual –OH groups on the hydrous amorphous TiO_2. The second weight loss ranging from 305.9 to 416 °C is assigned to the crystallization of anatase [60].

Tunable thickness of the TiO_2 coating of core–shell α-Fe_2O_3@TiO_2 nanorods

The shell thickness might be adjusted by changing the amount of TBOT (0.5 mL, 1.0 mL and 1.5 mL TBOT, labeled as α-FeOOH@TiO_2-0.5, α-FeOOH@TiO_2-1 and α-FeOOH@TiO_2-1.5, respectively). In Fig. 4b and c, core–shell α-FeOOH@TiO_2-1 and α-FeOOH@TiO_2-1.5 show a certain degree of conglutination and aggregation. In Fig. 5a–c, TEM images of α-FeOOH@TiO_2 composites display the increased coatings on the surface of α-FeOOH and the shells' thicknesses are about 10, 50, and 100 nm, respectively. After the calcination of α-FeOOH@TiO_2 composites, TEM images of α-Fe_2O_3@TiO_2 composites (labeled as α-Fe_2O_3@TiO_2-0.5, α-Fe_2O_3@TiO_2-1, α-Fe_2O_3@TiO_2-1.5) are shown in Fig. 4d–f. After the calcination, the conglutination and aggregation become heavier (Fig. 4e, f). In Fig. 5d–f, it is clearly shown that the shell thickness of TiO_2 equals to the corresponding thickness of amorphous TiO_2 coating. Moreover, with the increase of thickness of amorphous TiO_2 coating, α-Fe_2O_3 nanorods are packed by large amounts of TiO_2 nanoparticles to form the core–shell structure. Compared with the α-Fe_2O_3@TiO_2-0.75 (Fig. 1c), the thicknesses of the TiO_2 shells increase markedly and the shells of TiO_2 become much more compact (Fig. 5e, f). Therefore, the shell's thickness of

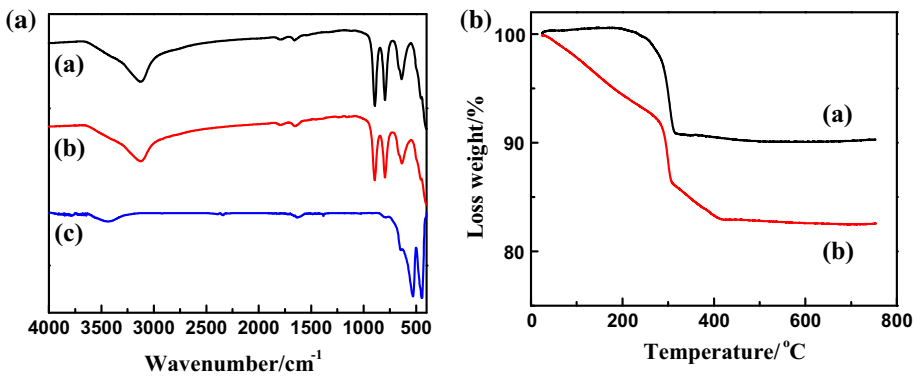

Fig. 3 **a** FTIR of *a* α-FeOOH, *b* α-FeOOH@TiO_2-0.75, *c* α-Fe_2O_3@TiO_2-0.75. **b** TG curves of *a* α-FeOOH and *b* α-FeOOH@TiO_2-0.75

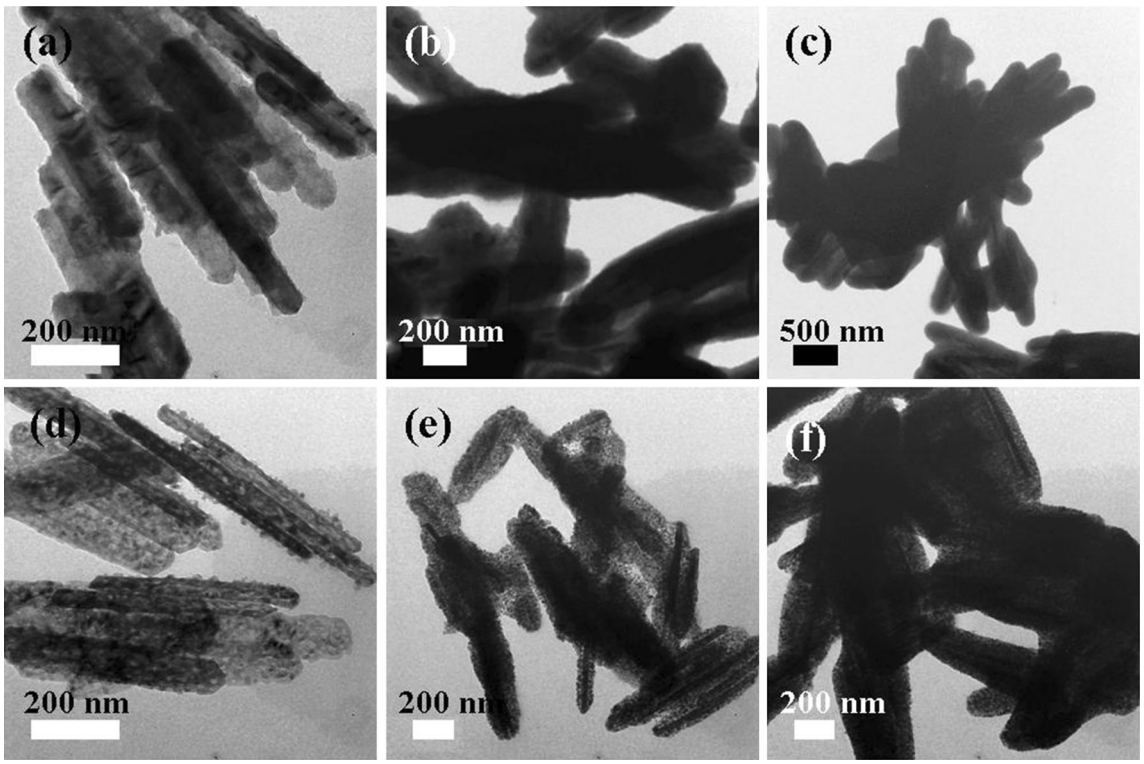

Fig. 4 TEM images of **a** α-FeOOH@TiO_2-0.5, **b** α-FeOOH@TiO_2-1, **c** α-FeOOH@TiO_2-1.5, **d** α-Fe_2O_3@TiO_2-0.5, **e** α-Fe_2O_3@TiO_2-1, **f** α-Fe_2O_3@TiO_2-1.5

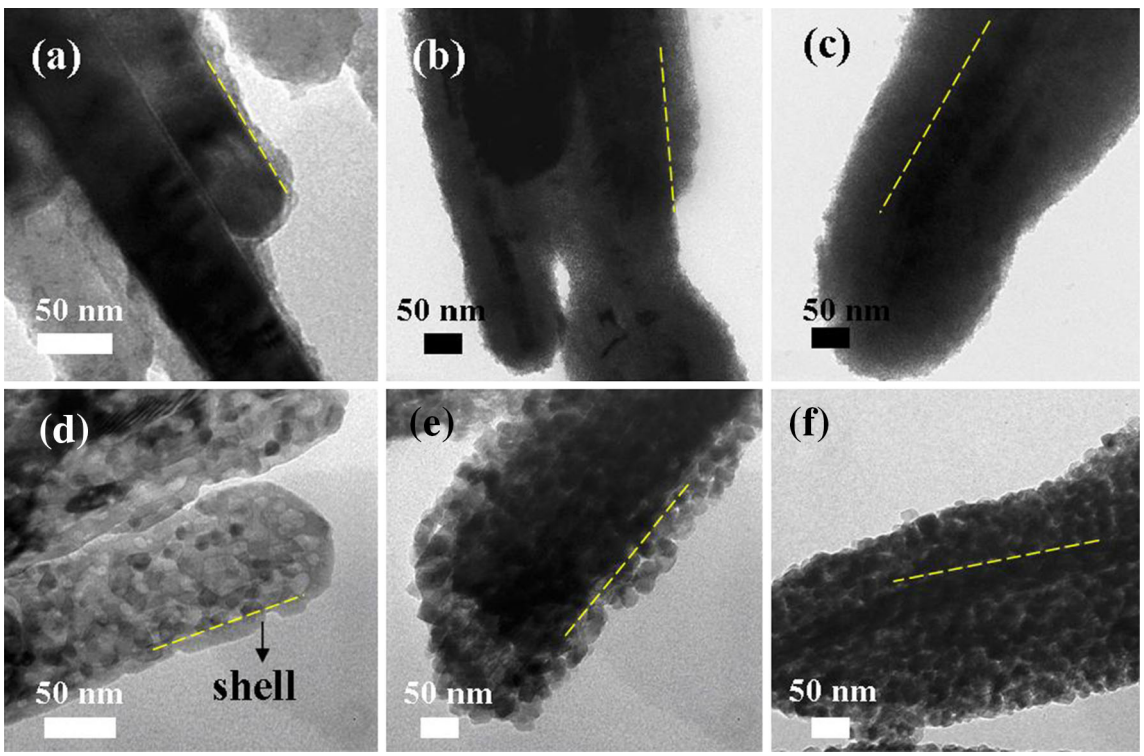

Fig. 5 TEM images with larger amplification of **a** α-FeOOH@TiO_2-0.5, **b** α-FeOOH@TiO_2-1, **c** α-FeOOH@TiO_2-1.5, **d** α-Fe_2O_3@TiO_2-0.5, **e** α-Fe_2O_3@TiO_2-1, **f** α-Fe_2O_3@TiO_2-1.5

core–shell α-Fe_2O_3@TiO_2 nanorods could be effectively controlled by varying the amount of TBOT.

XRD data further demonstrate that the chemical compositions of these samples are α-Fe_2O_3@TiO_2 composites (Fig. 6). Evidently, with the increase of the thickness of the TiO_2 layer, the intensity of these TiO_2 peaks enhance gradually. Additionally, in curve c and d, the peak at 27.4° is assigned to the (110) diffraction of rutile TiO_2 (JCPDS Card No. 21-1276) and the peak intensity increases with the increase of the content of Ti. To confirm the composition of α-Fe_2O_3@TiO_2 composites and the content of TiO_2 in the composites, EDX is used to characterize α-Fe_2O_3@TiO_2 composites and the result is shown in Fig. 7. EDX spectra showed that the main elemental compositions of nanocomposites are Fe, Ti, and O. The atom ratios Ti:Fe of α-Fe_2O_3@TiO_2-0.5, α-Fe_2O_3@TiO_2-0.75, α-Fe_2O_3@-TiO_2-1, and α-Fe_2O_3@TiO_2-1.5 are determined to be 1:9.9, 1:2.8, 1:1.8, and 1:0.72, respectively, which are consistent with the increase of the shells thickness. The corresponding weight fractions of TiO_2 in four composites are 9.1, 26.3, 35.7, and 58.1 %, respectively.

Figure 8a shows the diffuse reflectance spectra (DRS) of (a) TiO_2, (b) α-FeOOH, (c) α-Fe_2O_3, (d) α-Fe_2O_3@TiO_2-0.5, (e) α-Fe_2O_3@TiO_2-0.75, (f) α-Fe_2O_3@TiO_2-1, and (g) α-Fe_2O_3@TiO_2-1.5. In curve a, pure TiO_2 only absorbs ultraviolet radiation of less than 400 nm. Pure α-FeOOH shows the visible light absorption property (curve b). Compared with TiO_2 and α-FeOOH, α-Fe_2O_3 displays not only stronger absorption in the ultraviolet region of less than 400 nm but also adequate and strong absorption in the visible light region of 400–900 nm (curve c). From curve d to curve g, when TiO_2 was coated on the surface of α-Fe_2O_3, α-Fe_2O_3@TiO_2 composites show the similar the absorption properties as to α-Fe_2O_3. With the increase of TiO_2 amount, the absorption in the visible light region is decreased. The band gap energy of the samples can be confirmed by roughly comparing to the plot in Fig. 8b, which is obtained via the transformation based on the Kubelka–Munk function [58]. In Fig. 8b, A is the absorbance, h is the Planck constant, and v is the light frequency. According to the function, the estimated band gap values of TiO_2, α-FeOOH, α-Fe_2O_3, and α-Fe_2O_3@TiO_2-1.5 are 3.30 eV, 2.26 eV, 2.05 eV, and 2.10 eV, respectively. The band gap values of other α-Fe_2O_3@TiO_2 nanocomposites are between α-Fe_2O_3 and α-Fe_2O_3@TiO_2-1.5, which indicate that α-Fe_2O_3@TiO_2 nanocomposites may be a better candidate for photocatalysts in terms of utilization of visible solar light.

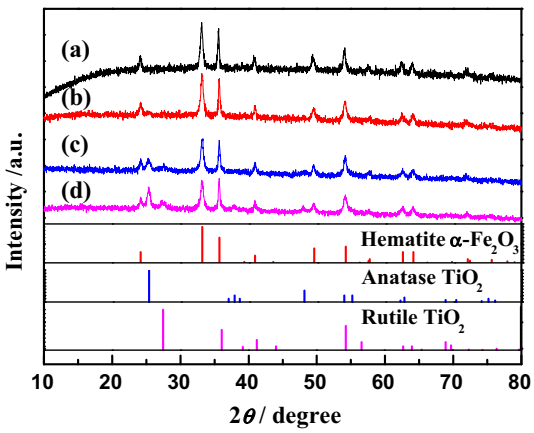

Fig. 6 XRD patterns for α-Fe_2O_3@TiO_2 obtained with different thickness TiO_2 shells. *a* α-Fe_2O_3@TiO_2-0.5, *b* α-Fe_2O_3@TiO_2-0.75, *c* α-Fe_2O_3@TiO_2-1, *d* α-Fe_2O_3@TiO_2-1.5. The *vertical lines* are the standard XRD patterns of hematite α-Fe_2O_3 (JCPDS Card No. 33-0664) (*red line*), anatase TiO_2 (JCPDS Card No. 21-1272) (*blue line*), and rutile TiO_2 (JCPDS Card No. 21-1276) (*magenta line*) (Color figure online)

Effect of calcination temperature

The effect of calcination temperature was studied. In typical reaction, α-FeOOH@TiO_2-0.75 composites were calcinated at 500 °C for 3 h. Then, the calcination process proceeded at 400, 600, 700, and 800 °C, respectively. The morphologies of these products are shown in Fig. 8. It is obvious that a lot of TiO_2 nanoparticles adsorb on the surface of α-Fe_2O_3 at 400 °C (in Fig. 9a). Furthermore, some hollows appear on the surface of nanorods. At 600 °C, TiO_2 nanoparticles are coated on the surface of α-Fe_2O_3 nanorods, forming compact TiO_2 nanoparticles shell (in Fig. 9b). At higher temperature (700 °C), the number of TiO_2 nanoparticles decreases and TiO_2 nanoparticles are congregated and fused to form TiO_2 shell (in Fig. 9c). When the calcination temperature is 800 °C, TiO_2 nanoparticles disappear from the surface of α-Fe_2O_3 nanorods owing to the fusion of TiO_2 nanoparticles to fabricate the intact and smooth TiO_2 shell. The crystal structure of the samples obtained at different calcination temperature was examined using XRD and the results are shown in Fig. 10. With the increase of calcination temperature, the crystalline structure of TiO_2 have changed from anatase to rutile titania. XRD patterns show that the position and relative intensity of diffraction peaks are in accordance with rhombohedral Fe_2O_3 and anatase or rutile titania, which confirms that the products are α-Fe_2O_3@-TiO_2 composites.

Photocatalytic performance of core–shell α-Fe_2O_3@TiO_2 nanorods

To evaluate the photocatalytic property of the as-prepared core–shell α-Fe_2O_3@TiO_2 nanorods, the photocatalytic degradation of RhB under the irradiation of UV light and visible light is chosen as a model reaction. Pure α-Fe_2O_3

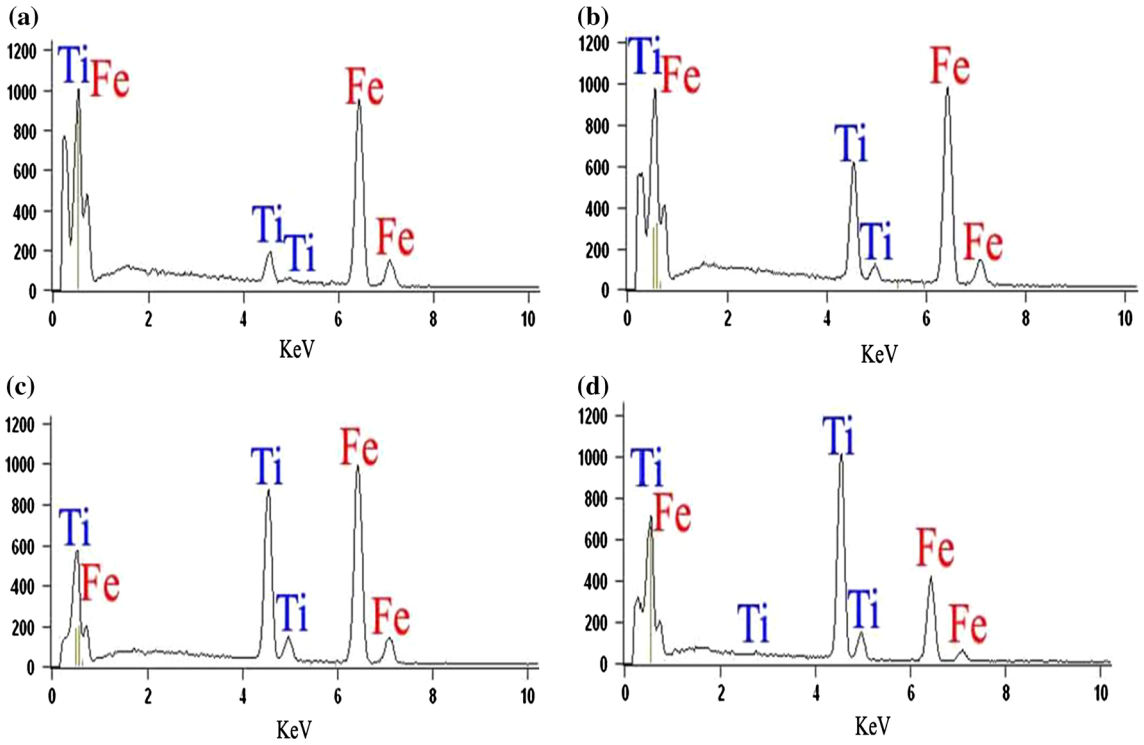

Fig. 7 EDX spectra of samples **a** α-Fe_2O_3@TiO_2-0.5, **b** α-Fe_2O_3@TiO_2-0.75, **c** α-Fe_2O_3@TiO_2-1, **d** α-Fe_2O_3@TiO_2-1.5

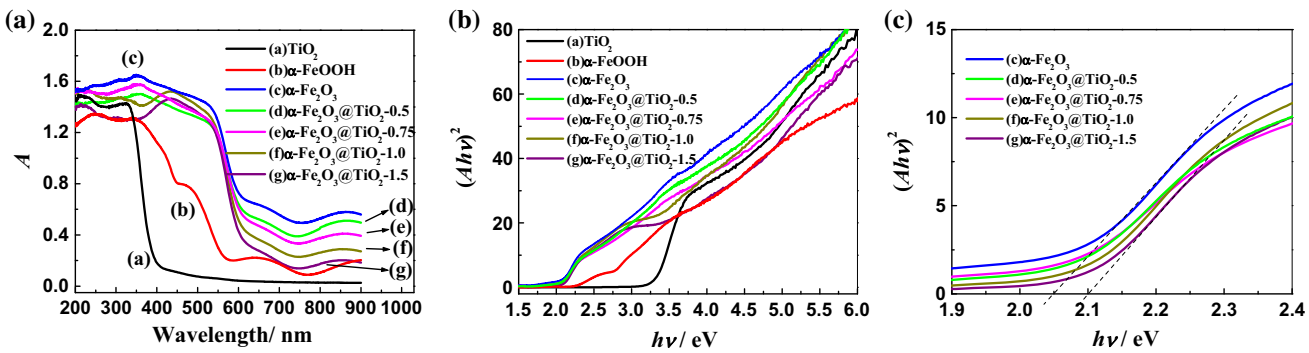

Fig. 8 **a** The UV–Vis diffuse reflectance spectra (DRS) of the *a* TiO_2, *b* α-FeOOH, *c* α-Fe_2O_3, *d* α-Fe_2O_3@TiO_2-0.5, *e* α-Fe_2O_3@TiO_2-0.75, *f* α-Fe_2O_3@TiO_2-1, and *g* α-Fe_2O_3@TiO_2-1.5. **b**, **c** The plot of $(Ahv)^2$ versus *hv*

nanorods have no photocatalytic activity under the irradiation of UV light. From Fig. 11, it is clearly found that the concentration of RB decreased rapidly under the irradiation of UV light, in accordance with the photos of sample with different irradiation time (insert of Fig. 11a, b). The whole decolorization process required 150 min in the presence of two α-Fe_2O_3@TiO_2 composites. The linear relations between $\ln(c_t/c_0)$ and reaction time by different catalysts under irradiation of UV light are displayed in Fig. 12a, from which the reaction rate constants are calculated and listed in Table 1. As displayed in Table 1, the α-Fe_2O_3@TiO_2-1 under the conditions displays the highest rate constant (ca. 0.030 min^{-1}) among all the samples. It is found that the thickness of TiO_2 shell affects the photocatalytic properties of α-Fe_2O_3@TiO_2 composites. The increase of rate constant is not proportional to the shell thickness. With the increase of TiO_2 thickness, the rate constants reach the saturation.

The photocatalytic activity for the α-Fe_2O_3@TiO_2 core–shell nanorods was also evaluated under the irradiation of visible light. The linear relations between $\ln(c_t/c_0)$ and reaction time are displayed in Fig. 12b. The reaction rate constants are calculated and listed in Table 1. Pure α-Fe_2O_3 nanorods also have no photocatalytic activity under the irradiation of visible light. Pure TiO_2 powder shows slow reaction rate under the irradiation of visible light due to its

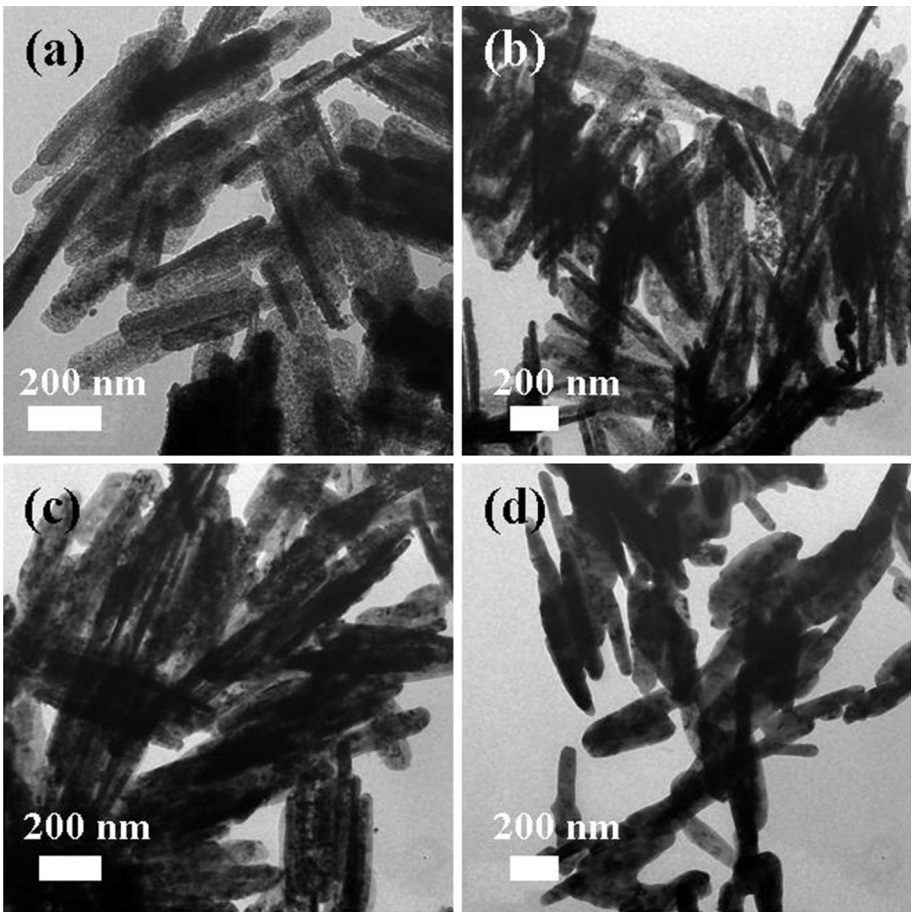

Fig. 9 TEM images of the α-FeOOH@TiO_2-0.75 after calcination at **a** 400 °C, **b** 600 °C, **c** 700 °C, and **d** 800 °C for 3 h

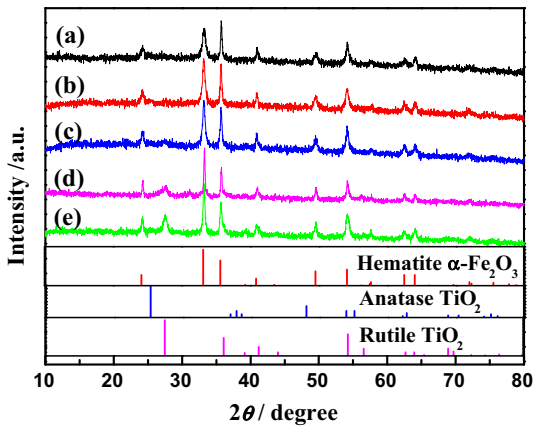

Fig. 10 XRD patterns of α-FeOOH@TiO_2-0.75 calcined at different temperatures for 3 h, *a* 400 °C, *b* 500 °C, *c* 600 °C, *d* 700 °C, *e* 800 °C. The *vertical lines* are the standard XRD patterns of hematite α-Fe_2O_3 (JCPDS Card No. 33-0664) (*red line*), anatase TiO_2 (JCPDS Card No. 21-1272) (*blue line*), and rutile TiO_2 (JCPDS Card No. 21-1276) (*magenta line*) (Color figure online)

narrow absorption region. However, the reaction constant of α-Fe_2O_3@TiO_2-1 is about 2.5 times that of pure TiO_2 powder. In addition, the reaction rate constants obtained under the irradiation of visible light are smaller than those under the irradiation of UV light, which is attributed to rapid generation electron–hole pairs of TiO_2 shell under the irradiation of UV light. α-Fe_2O_3 core cannot affect the UV light absorption of TiO_2 shell. On the contrary, in core–shell structure of TiO_2@α-Fe_2O_3, the α-Fe_2O_3 shell will adsorb some UV light and block rapid generation electron–hole pairs of TiO_2 core [50]. The main charge-transfer processes between TiO_2 shell and α-Fe_2O_3 core, as shown in Fig. 13, might clarify the improved visible light photocatalytic activity of α-Fe_2O_3@TiO_2 composites. Under the visible light irradiation, TiO_2 shell cannot absorb the visible light (Fig. 8a, curve a), resulting in no generation of electron–hole pairs. However, α-Fe_2O_3 core can be easily excited and generate charge carriers. Then, the photogenerated electrons transfer from the conduction band (CB) of α-Fe_2O_3 to CB of TiO_2 under the effect of built-in electric field and the concentration gradient of electrons, while photogenerated holes accumulate in the valence band (VB) of α-Fe_2O_3 [55, 56, 58]. The negative electrons in CB of TiO_2 will further react with molecular oxygen O_2 dissolved in the RhB solution to generate the superoxide anion O_2^-. On the other hand, the accumulated holes in VB of α-Fe_2O_3

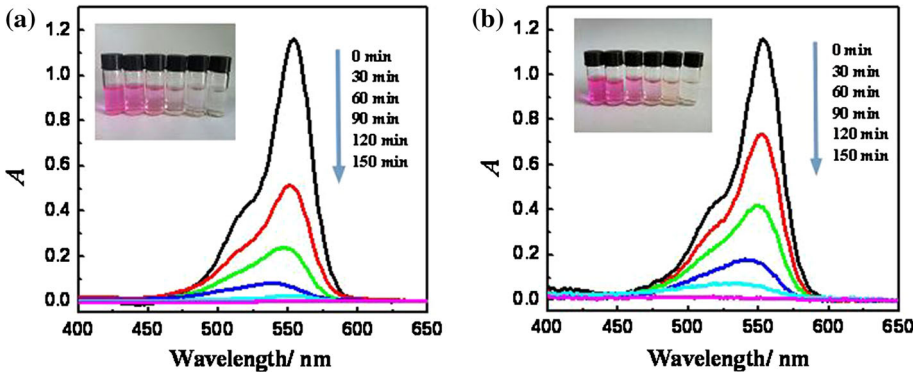

Fig. 11 Absorption spectra of a solution of RB (1.5×10^{-5} M, 100 mL) in the presence of 50 mg of **a** α-Fe_2O_3@TiO_2-0.75, **b** α-Fe_2O_3@TiO_2-1.5 under exposure to UV light

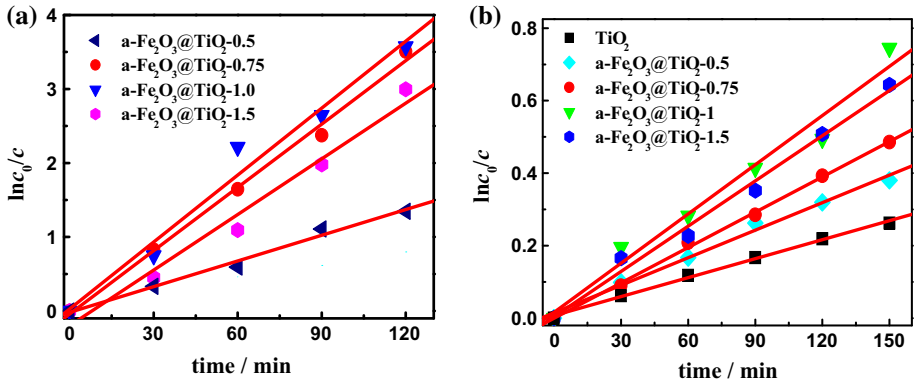

Fig. 12 First-order kinetic plot of RhB degradation catalyzed by different catalysts under irradiation of **a** UV light and **b** visible light

Table 1 Comparison of Photocatalytic performances of various catalysts for photocatalytic degradation of RhB

Catalyst	Reaction rate constant ($k \times 10^3$/min^{-1})	
	UV light irradiation	Visible light irradiation
TiO_2	–	1.8 ± 0.3
α-Fe_2O_3@TiO_2-0.5	11.7 ± 0.9	2.5 ± 0.2
α-Fe_2O_3@TiO_2-0.75	27.3 ± 1.1	3.3 ± 0.3
α-Fe_2O_3@TiO_2-1	29.8 ± 0.7	4.5 ± 0.4
α-Fe_2O_3@TiO_2-1.5	25.4 ± 1.2	4.2 ± 0.3

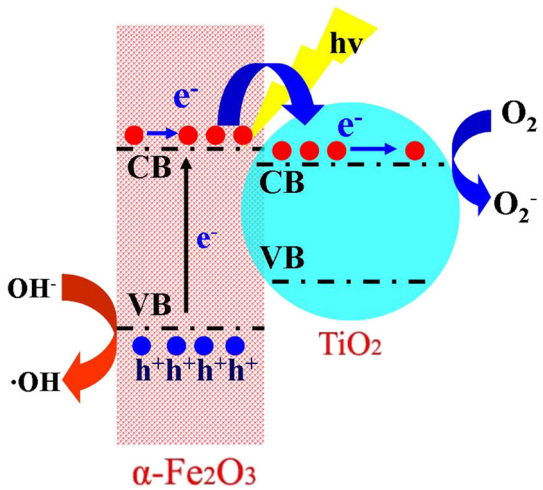

Fig. 13 Schematic illustrating the charge-transfer process between TiO_2 shell and α-Fe_2O_3 core under visible light irradiation

will react with OH^- species, generating reactive hydroxyl radicals (·OH) [55, 56, 58]. Therefore, core–shell α-Fe_2O_3@TiO_2 composites show the efficient photocatalytic activity in visible light region. The reaction constants of core–shell α-Fe_2O_3@TiO_2 composites are smaller than those reported in recent literatures [61–65], which might be attributed to the different reaction conditions, such as the initial concentration, catalysts dosage.

The photocatalytic activities for the core–shell α-Fe_2O_3@TiO_2-0.75 nanorods obtained at different calcination temperature were also evaluated under the irradiation of UV light. The linear relations between $\ln(c_t/c_0)$ and reaction time are displayed in Fig. 14. From 400 °C to 800 °C, the kinetic rate constants are 11.4, 28.5, 25.4, 8.5, and 5.6 min^{-1}, respectively. Obviously, α-Fe_2O_3@TiO_2-0.75 nanorods obtained at 500 °C exhibit the best photocatalytic activity, because anatase titania has higher photocatalytic activity than rutile titania [66]. With the increase of the calcination temperature, the transformation of crystalline structure of TiO_2 from anatase to rutile titania leads to the

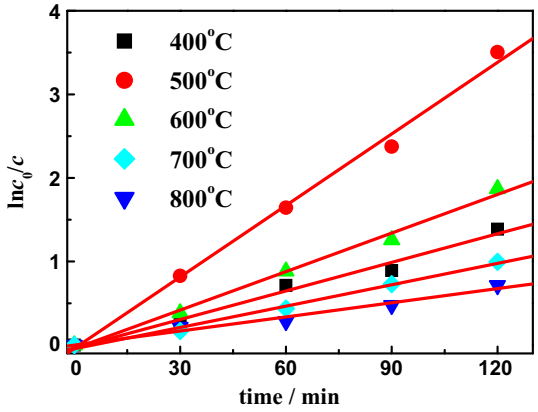

Fig. 14 First-order kinetic plot of RhB degradation catalyzed by α-Fe_2O_3@TiO_2-0.75 nanocomposites prepared at different calcination temperature under irradiation of UV light

decline of photocatalytic activities (in Fig. 14). Furthermore, the morphology change of TiO_2 shell affects photocatalytic property. At high calcination temperature, TiO_2 nanoparticles are fused to form the intact and compact TiO_2 shell (Fig. 9), causing the fast electron–hole recombination rate. On the contrary, at relative low calcination temperature, TiO_2 shells are made up of small nanoparticles, which have a large number of grain boundaries and interfaces on the surface of α-Fe_2O_3 core, slowing down electron–hole recombination rate. Therefore, through the catalytic performance test, the photocatalytic performances of core–shell α-Fe_2O_3@TiO_2 composites heavily depend on the thickness, density, and crystal structure of TiO_2 coating shells.

Conclusions

In conclusion, novel core–shell α-Fe_2O_3@TiO_2 nanorods with different shell thicknesses were synthesized using α-FeOOH nanorods as hard templates. The core–shell α-Fe_2O_3@TiO_2 composites exhibited the excellent optical response and photocatalytic activity from the ultraviolet to the visible region. The tunable photocatalytic activities are attributed to the adjustable TiO_2 shells of core–shell α-Fe_2O_3@TiO_2 composites. The α-Fe_2O_3@TiO_2-1 displayed the best photocatalytic activity under both UV light and visible light. The anatase titania has the higher photocatalytic activity. The proposed synthesis strategy might provide a facile and effective method for developing noble semiconductors core–shell heterojunction nanocomposites.

Acknowledgements This work was financially supported by the National Natural Science Foundation of China (Grant No. 21273195), and a Project Funded by the Priority Academic Program Development of Jiangsu Higher Education Institutions. The work was also sponsored by Qing Lan Project of Higher Learning Institutions in Jiangsu Province, the support of high-end talent plan of Yangzhou university, and Jiangsu Key Laboratory of Environmental Material and Environmental Engineering (K11032, K13062). The authors also acknowledge the Testing Center of Yangzhou University for TEM, SEM, XRD, and EDX experiments.

References

1. Bach U, Lupo D, Comte P, Moser JE, Weissörtel F, Salbeck J, Spreitzer H, Grätzel M (1998) Solid-state dye-sensitized mesoporous TiO_2 solar cells with high photon-to-electron conversion efficiencies. Nature 395:583–585
2. Péchy P, Renouard T, Zakeeruddin SM, Humphry-Baker R, Comte P, Liska P, Cevey L, Costa E, Shklover V, Spiccia L, Deacon GB, Bignozzi CA, Grätzel M (2001) Engineering of efficient panchromatic sensitizers for nanocrystalline TiO_2-based solar cells. J Am Chem Soc 123:1613–1624
3. Konstantinou IK, Albanis TA (2004) TiO_2-assisted photocatalytic degradation of azo dyes in aqueous solution: kinetic and mechanistic investigations: a review. Appl Catal B 49:1–14
4. Han F, Kambala VSR, Srinivasan M, Rajarathnam D, Naidu R (2009) Tailored titanium dioxide photocatalysts for the degradation of organic dyes in wastewater treatment: a review. Appl Catal A 359:25–40
5. Gaya UI, Abdullah AH (2008) Heterogeneous photocatalytic degradation of organic contaminants over titanium dioxide: a review of fundamentals, progress and problems. J Photochem Photobiol C 9:1–12
6. Henderson MA (2011) A surface science perspective on photocatalysis. Surf Sci Rep 66:185–297
7. Hernández-Alonso MD, Fresno F, Suárez S, Coronado JM (2009) Development of alternative photocatalysts to TiO_2: challenges and opportunities. Energy Environ Sci 2:1231–1257
8. Wold A (1993) Photocatalytic properties of titanium dioxide (TiO_2). Chem Mater 5:280–283
9. Anpo M, Takeuchi M (2003) The design and development of highly reactive titanium oxide photocatalysts operating under visible light irradiation. J Catal 216:505–516
10. Chen C, Ma W, Zhao J (2010) Semiconductor-mediated photodegradation of pollutants under visible-light irradiation. Chem Soc Rev 39:4206–4219
11. Nakamura I, Negishi N, Kutsuna S, Ihara T, Sugihara S, Takeuchi K (2000) Role of oxygen vacancy in the plasma-treated TiO_2 photocatalyst with visible light activity for NO removal. J Mol Catal Chem 161:205–212
12. Diwald O, Thompson TL, Zubkov T, Walck SD, Yates JT (2004) Photochemical activity of nitrogen-doped rutile TiO_2(110) in visible light. J Phys Chem B 108:6004–6008
13. Agrios AG, Pichat P (2006) Recombination rate of photogenerated charges versus surface area: opposing effects of TiO_2 sintering temperature on photocatalytic removal of phenol, anisole, and pyridine in water. J Photochem Photobiol Chem 180:130–135
14. Shkrob IA, Sauer MC (2004) Hole scavenging and photo-stimulated recombination of electron–hole pairs in aqueous TiO_2 nanoparticles. J Phys Chem B 108:12497–12511
15. Berger T, Sterrer M, Diwald O, Knözinger E, Panayotov D, Thompson TL, Yates JT (2005) Light-induced charge separation in anatase TiO_2 particles. J Phys Chem B 109:6061–6068
16. Litter MI (1999) Heterogeneous photocatalysis: transition metal ions in photocatalytic systems. Appl Catal B 23:89–114
17. Dvoranová D, Brezová V, Mazúr M, Malati MA (2002) Investigations of metal-doped titanium dioxide photocatalysts. Appl Catal B 37:91–105

18. Chang S, Liu W (2014) The roles of surface-doped metal ions (V, Mn, Fe, Cu, Ce, and W) in the interfacial behavior of TiO_2 photocatalysts. Appl Catal B 156–157:466–475
19. Huang SY, Schlichthörl G, Nozik AJ, Grätzel M, Frank AJ (1997) Charge recombination in dye-sensitized nanocrystalline TiO_2 solar cells. J Phys Chem B 101:2576–2582
20. Mor GK, Shankar K, Paulose M, Varghese OK, Grimes CA (2006) Use of highly-ordered TiO_2 nanotube arrays in dye-sensitized solar cells. Nano Lett 6:215–218
21. Subramanian V, Wolf EE, Kamat PV (2004) Catalysis with TiO_2/Gold nanocomposites. Effect of metal particle size on the fermi level equilibration. J Am Chem Soc 126:4943–4950
22. Hirakawa T, Kamat PV (2005) Charge separation and catalytic activity of Ag@TiO_2 core–shell composite clusters under UV–Irradiation. J Am Chem Soc 127:3928–3934
23. Dawson A, Kamat PV (2001) Semiconductor–metal nanocomposites. Photoinduced fusion and photocatalysis of gold-capped TiO_2 (TiO_2/Gold) nanoparticles. J Phys Chem B 105:960–966
24. Gomes Silva C, Juárez R, Marino T, Molinari R, García H (2011) Influence of excitation wavelength (UV or Visible light) on the photocatalytic activity of titania Containing gold nanoparticles for the generation of hydrogen or oxygen from water. J Am Chem Soc 133:595–602
25. Murdoch M, Waterhouse GIN, Nadeem MA, Metson JB, Keane MA, Howe RF, Llorca J, Idriss H (2011) The effect of gold loading and particle size on photocatalytic hydrogen production from ethanol over Au/TiO_2 nanoparticles. Nat Chem 3:489–492
26. Li XZ, Li FB, Yang CL, Ge WK (2001) Photocatalytic activity of WO_x-TiO_2 under visible light irradiation. J Photochem Photobiol Chem 141:209–217
27. Sajjad AKL, Shamaila S, Tian B, Chen F, Zhang J (2009) One step activation of WO_x/TiO_2 nanocomposites with enhanced photocatalytic activity. Appl Catal B 91:397–405
28. Li Y, Zhang H, Guo Z, Han J, Zhao X, Zhao Q, Kim SJ (2008) Highly efficient visible-light-induced photocatalytic activity of nanostructured AgI/TiO_2 photocatalyst. Langmuir 24:8351–8357
29. Bessekhouad Y, Robert D, Weber JV (2004) Bi_2S_3/TiO_2 and CdS/TiO_2 heterojunctions as an available configuration for photocatalytic degradation of organic pollutant. J Photochem Photobiol Chem 163:569–580
30. Yu J, Dai G, Huang B (2009) Fabrication and characterization of visible-light-driven plasmonic photocatalyst Ag/AgCl/TiO_2 nanotube arrays. J Phys Chem C 113:16394–16401
31. Vinodgopal K, Bedja I, Kamat PV (1996) Nanostructured Semiconductor films for photocatalysis. photoelectrochemical behavior of SnO_2/TiO_2 composite systems and its role in photocatalytic degradation of a textile azo dye. Chem Mater 8:2180–2187
32. Du J, Qi J, Wang D, Tang Z (2012) Facile synthesis of Au@TiO_2 core–shell hollow spheres for dye-sensitized solar cells with remarkably improved efficiency. Energy Environ Sci 5:6914–6918
33. Alayoglu S, Nilekar AU, Mavrikakis M, Eichhorn B (2008) Ru–Pt core–shell nanoparticles for preferential oxidation of carbon monoxide in hydrogen. Nat Mater 7:333–338
34. Zhao Y, Meng Y, Jiang P (2014) Carbon@MnO_2 core–shell nanospheres for flexible high-performance supercapacitor electrode materials. J Power Sources 259:219–226
35. Chen M, Li W, Shen X, Diao G (2014) Fabrication of core–shell α-Fe2O3@ Li4Ti5O12 composite and its application in the lithium ion batteries. ACS Appl Mater Interfaces 6:4514–4523
36. Xue X, Xing L, Chen Y, Shi S, Wang Y, Wang T (2008) Synthesis and H_2S sensing properties of CuO–SnO_2 core/shell PN-junction nanorods. J Phys Chem C 112:12157–12160
37. Sertchook H, Avnir D (2003) Submicron silica/polystyrene composite particles prepared by a one-step sol–gel process. Chem Mater 15:1690–1694
38. Zhou W, Cao X, Zeng Z, Shi W, Zhu Y, Yan Q, Liu H, Wang J, Zhang H (2013) One-step synthesis of Ni_3S_2 nanorod@$Ni(OH)_2$ nanosheet core–shell nanostructures on a three-dimensional graphene network for high-performance supercapacitors. Energy Environ Sci 6:2216–2221
39. Xu C, Yuan Y, Cui A, Yuan R (2012) In situ controllable synthesis of Ag@AgCl core–shell nanoparticles on graphene oxide sheets. J Mater Sci 48:967–973. doi:10.1007/s10853-012-6823-2
40. Hossain MM, Shima H, Ku B-C, Hahn JR (2014) Nanoforests composed of ZnO/C core–shell hexagonal nanosheets: fabrication and growth in a sealed thermolysis reactor and optical properties. J Mater Sci 50:93–103. doi:10.1007/s10853-014-8569-5
41. Chen LY, Fujita T, Ding Y, Chen MW (2010) A three-dimensional gold-decorated nanoporous copper core–shell composite for electrocatalysis and nonenzymatic biosensing. Adv Funct Mater 20:2279–2285
42. Zhao W, Du N, Xiao C, Wu H, Zhang H, Yang D (2014) Large-scale synthesis of Ag–Si core–shell nanowall arrays as high-performance anode materials of Li-ion batteries. J Mater Chem A 2:13949–13954
43. Leary R, Westwood A (2011) Carbonaceous nanomaterials for the enhancement of TiO_2 photocatalysis. Carbon 49:741–772
44. Williams G, Seger B, Kamat PV (2008) TiO_2-graphene nanocomposites. UV-assisted photocatalytic reduction of graphene oxide. ACS Nano 2:1487–1491
45. Vinodgopal K, Kamat PV (1995) Enhanced rates of photocatalytic degradation of an azo dye using SnO_2/TiO_2 coupled semiconductor thin films. Environ Sci Technol 29:841–845
46. Liu Z, Sun DD, Guo P, Leckie JO (2007) An efficient bicomponent TiO_2/SnO_2 nanofiber photocatalyst fabricated by electrospinning with a side-by-side dual spinneret method. Nano Lett 7:1081–1085
47. Li J, Chen J, Ke R, Luo C, Hao J (2007) Effects of precursors on the surface Mn species and the activities for NO reduction over MnO_x/TiO_2 catalysts. Catal Commun 8:1896–1900
48. Somasundaram S, Chenthamarakshan CR, de Tacconi NR, Ming Y, Rajeshwar K (2004) Photoassisted deposition of chalcogenide semiconductors on the titanium dioxide surface: mechanistic and other aspects. Chem Mater 16:3846–3852
49. Kay A, Cesar I, Grätzel M (2006) New benchmark for water photooxidation by nanostructured α-Fe_2O_3 films. J Am Chem Soc 128:15714–15721
50. Zhong LS, Hu JS, Liang HP, Cao AM, Song WG, Wan LJ (2006) Self-assembled 3D flowerlike iron oxide nanostructures and their application in water treatment. Adv Mater 18:2426–2431
51. Wei Z, Xing R, Zhang X, Liu S, Yu H, Li P (2013) Facile template-free fabrication of hollow nestlike α-Fe_2O_3 nanostructures for water treatment. ACS Appl Mater Interfaces 5:598–604
52. Sun L, Wu W, Yang S, Zhou J, Hong M, Xiao X, Ren F, Jiang C (2014) Template and silica interlayer tailorable synthesis of spindle-like multilayer α-Fe_2O_3/Ag/SnO_2 ternary hybrid architectures and their enhanced photocatalytic activity. ACS Appl Mater Interfaces 6:1113–1124
53. Wu W, Zhang S, Xiao X, Zhou J, Ren F, Sun L, Jiang C (2012) Controllable synthesis, magnetic properties, and enhanced photocatalytic activity of spindlelike mesoporous α-Fe2O3/ZnO core–shell heterostructures. ACS Appl Mater Interfaces 4:3602–3609
54. Shi Y, Li H, Wang L, Shen W, Chen H (2012) Novel α-Fe_2O_3/CdS cornlike nanorods with enhanced photocatalytic performance. ACS Appl Mater Interfaces 4:4800–4806
55. Peng L, Xie T, Lu Y, Fan H, Wang D (2010) Synthesis, photoelectric properties and photocatalytic activity of the Fe_2O_3/TiO_2 heterogeneous photocatalysts. Phys Chem Chem Phys 12: 8033–8041
56. Wu Q, Ouyang J, Xie K, Sun L, Wang M, Lin C (2012) Ultrasound-assisted synthesis and visible-light-driven photocatalytic

activity of Fe-incorporated TiO_2 nanotube array photocatalysts. J Hazard Mater 199–200:410–417
57. Tang H, Zhang D, Tang G, Ji X, Li W, Li C, Yang X (2013) Hydrothermal synthesis and visible-light photocatalytic activity of α-Fe_2O_3/TiO_2 composite hollow microspheres. Ceram Int 39:8633–8640
58. Xia Y, Yin L (2013) Core–shell structured α-Fe_2O_3@TiO_2 nanocomposites with improved photocatalytic activity in the visible light region. Phys Chem Chem Phys 15:18627–18634
59. Li W, Yang J, Wu Z, Wang J, Li B, Feng S, Deng Y, Zhang F, Zhao D (2012) A versatile kinetics-controlled coating method to construct uniform porous TiO2 shells for multifunctional core–shell structures. J Am Chem Soc 134:11864–11867
60. Li GL, Wang GH (1999) Synthesis of nanometer-sized TiO_2 particles by a microemulsion method. Nanostructured Mater 11:663–668
61. Natarajan TS, Natarajan K, Bajaj HC, Tayade RJ (2013) Enhanced photocatalytic activity of bismuth-doped TiO_2 nanotubes under direct sunlight irradiation for degradation of Rhodamine B dye. J Nanoparticle Res 15:1–18
62. Dong F, Wang H, Wu Z (2009) One-step "green" synthetic approach for mesoporous C-doped titanium dioxide with efficient visible light photocatalytic activity. J Phys Chem C 113:16717–16723
63. Zhang Z, Shao C, Li X, Sun Y, Zhang M, Mu J, Zhang P, Guo Z, Liu Y (2012) Hierarchical assembly of ultrathin hexagonal SnS_2 nanosheets onto electrospun TiO_2 nanofibers: enhanced photocatalytic activity based on photoinduced interfacial charge transfer. Nanoscale 5:606–618
64. Liu C, Meng D, Li Y, Wang L, Liu Y, Luo S (2015) Hierarchical architectures of ZnS–In_2S_3 solid solution onto TiO2 nanofibers with high visible-light photocatalytic activity. J Alloys Compd 624:44–52
65. Boppella R, Basak P, Manorama SV (2012) Viable method for the synthesis of biphasic TiO_2 nanocrystals with tunable phase composition and enabled visible-light photocatalytic performance. ACS Appl Mater Interfaces 4:1239–1246
66. Sclafani A, Herrmann JM (1996) Comparison of the photoelectronic and photocatalytic activities of various anatase and rutile forms of titania in pure liquid organic phases and in aqueous solutions. J Phys Chem 100:13655–13661